Mineralium Deposita (2019) 54:849–866
https://doi.org/10.1007/s00126-018-0846-9

ARTICLE

Recent Mn-Ag deposits in coastal hydrothermal springs in the Baja California Peninsula, Mexico

Augusto Antonio Rodríguez-Díaz[1,2] · Carles Canet[2] · Ruth Esther Villanueva-Estrada[2] · Elizabeth Chacón[3] · Fernando Gervilla[4] · Fernando Velasco-Tapia[3] · Esther María Cruz-Gámez[3] · Eduardo González-Partida[5] · Raymundo Casas-García[6] · Carlos Linares-López[2] · Daniel Pérez-Zárate[2,7]

Received: 25 October 2017 / Accepted: 3 October 2018 / Published online: 23 October 2018

Abstract

Hot springs with associated Mn-Ag mineralization were identified in the intertidal zone of the Bahia Concepcion Bay of the central-eastern Baja California Peninsula. Hot spring activity is related to a system of NW-SE faults that are associated with the opening of the Gulf of California. The hot springs are hosted by Miocene volcanic and volcaniclastic units of the Comondu Group. The maximum discharge temperature recorded is 72 °C, with the pH ranging from 6.2 to 6.5 and salinity values reaching up to 27 g/kg. Veins, stockworks, breccias, crusts, and organosedimentary stromatolites of silica-carbonate and Mn oxides are associated with the hot springs. The Mn oxide and silica deposits show an association with Ag, As, Ba, Ca, Cu, Mg, Pb, Sb, Sr, Tl, V, W, and Zn. Acanthite and native silver occur along with pyrite in a mineral assemblage rich in opal-A, todorokite, romanechite, aragonite, high-Mg calcite, and barite. Three distinct mineral associations characterized by sulfides, sulfates, and oxides are recognized. The silver minerals formed late in the paragenesis. Textural evidence suggests a microbial mediation for the Mn mineral deposition. Pourbaix diagrams for Mn and Ag species were constructed for the physicochemical conditions of the coastal hot springs. These diagrams show that both Mn and Ag minerals are stable at low temperature (65 °C), and near neutral pH, under slightly reducing or oxidizing conditions. The characteristics of the subaerial to shallow submarine hot springs and the results of the geochemical modeling suggest that the hydrothermal system in the Bahia Conception Bay is formed through convection of meteoric waters, intermixed with some saline fluids or seawater.

Keywords Hot spring mineralization · Todorokite · Acanthite · Native silver · Mn-stromatolites · Gulf of California

Editorial handling: T. Monecke

Electronic supplementary material The online version of this article (https://doi.org/10.1007/s00126-018-0846-9) contains supplementary material, which is available to authorized users.

✉ Augusto Antonio Rodríguez-Díaz
augusto@geofisica.unam.mx

[1] Posgrado en Ciencias de la Tierra, Universidad Nacional Autónoma de México, Ciudad Universitaria, 04510 México City, Mexico

[2] Instituto de Geofísica, Universidad Nacional Autónoma de México, Ciudad Universitaria, 04510 México City, Mexico

[3] Facultad de Ciencias de la Tierra, Ex-Hacienda de Guadalupe, Universidad Autónoma de Nuevo León, Carretera Linares-Cerro Prieto km 8, 67700 Linares, Nuevo León, Mexico

[4] Departamento de Mineralogía y Petrología and Instituto Andaluz de Ciencias de la Tierra, Facultad de Ciencias, Universidad de Granada-CSIC, Av. Fuentenueva s/n, 18002 Granada, Spain

[5] Centro de Geociencias, Universidad Nacional Autónoma de México, Blvd. Juriquilla 3001, Juriquilla, 76230 Querétaro, Mexico

[6] Institut für Geologie, Technische Universität Bergakademie Freiberg, Bernhard-von-Cotta-Str. 2, 09599 Freiberg, Germany

[7] CONACYT-Instituto de Geofísica, Universidad Nacional Autónoma de México, Ciudad Universitaria, 04510 México City, Mexico

Introduction

Modern Mn oxide deposits formed by hot springs have been reported in shallow and deep marine and continental environments (Hewett 1968; Miura and Hariya 1997; Canet et al. 2005; Hein et al. 2005). The deposits are typically hosted by volcanic rocks formed in extensional regimes (Liakopoulos et al. 2001; Camprubí et al. 2008; Sinisi et al. 2012; Kanellopoulos et al. 2017). These deposits, as well as older, related Mn deposits, can exhibit enrichment in Ag (Nicholson 1992; Hein et al. 2005). However, their geochemical and mineralogical characteristics and the processes of deposition are not well-documented.

Hot spring systems are natural laboratories for studying fluid-rock interactions and mineralizing processes involved in the formation of Ag-Mn ore deposits. They provide critical information to constrain the deposit model and can be used to identify exploration vectors (Clark and Williams-Jones 1990; Leal et al. 2008; Camprubí et al. 2008). Moreover, these active hydrothermal systems are of special scientific interest because they support communities of extremophile organisms that mediate mineral precipitation (Usui and Mita 1995; Mita and Miura 2003; Tebo et al. 2004).

The Bahia Concepcion Bay (BC), located on the eastern coast of the central Baja California Peninsula in Mexico, is host to several coastal hydrothermal springs. These cluster in the Mapachitos area, where hot springs occur at depths of 5–15 m below sea level and in the intertidal zone, and along a ~0.8 km long strip of the coast at Posada Concepcion, where the discharge occurs in the intertidal zone. In both areas of discharge, there are stromatolite-like deposits of opal, calcite and Mn oxides, enriched in Ba, Hg, and As (Prol-Ledesma et al. 2004; Canet et al. 2005; Villanueva-Estrada et al. 2013).

In this paper, we report the occurrence of Ag minerals associated with Mn oxides in the coastal hot springs of the BC. Our findings provide new information on the mineralizing processes and physical-chemical conditions of Ag-Mn ore formation.

Geological setting

The studied hot springs are located on the west shore of the fault-bounded BC, ~17 km south of Mulege town along the central-eastern coast of Baja California Peninsula in Mexico (Fig. 1). Calc-alkaline volcanic, volcaniclastic, and intrusive rocks of the Oligocene-Miocene Comondu Group and minor Pliocene to Quaternary sedimentary rocks, lava flows, domes, and pyroclastic rocks are exposed along the shoreline (Fig. 1).

In the BC region, the Comondu Group is comprised, from bottom to top, of the El Salto, Pelones, Minitas, Pilares, Hornillos, and Ricason formations (Camprubí et al. 2008). The Ricason Formation (17–22 Ma) dominates the western side of the bay (Rodríguez-Díaz et al. 2008), where the hot springs are located (Fig. 1). The Ricason Formation consists of a succession of andesitic-basaltic lavas, andesitic ash-lapilli tuffs and andesitic breccias and agglomerates.

Three generations of faulting are recognized. Early ENE-WSW-trending, normal faults affected the basement and controlled the initial emplacement of the volcanic Comondu Group. Middle Miocene normal and strike-slip faults have a NNE-SSW trend and are related to the structural segmentation of the Main Gulf Escarpment. Finally, Late Miocene to Pliocene NW-SE normal faults and minor strike-slip faults are associated with the opening of the Gulf of California (Casarrubias-Unzueta and Gómez-López 1994). The main faults zones are the BC and El Requeson faults. These faults record reactivation events (Rodríguez-Díaz et al. 2008). These faults bound the bay in a NW-SE graben configuration developed during the late Miocene-Pliocene due to the extension that affected the Gulf of California (Rodríguez-Díaz et al. 2008). The BC Fault hosts Mn oxides veins (e.g., Guadalupe ore deposit, Terán-Ortega et al. 1993), whereas the El Requeson Fault controls the coastal hot springs in the area (Rodríguez-Díaz et al. 2008). As consequence, venting in the area occurs along by NW-SE fractures and faults, as well as the intersections of NW-SE and NE-SW faults (Fig. 1b).

Hydrothermal activity

BC has been identified as a region with high geothermal potential (Arango-Galván et al. 2015), with two main areas of geothermal interest: Mapachitos and Posada Concepcion (Fig. 1). Active hydrothermal activity occurs along the shore of the BC bay (Fig. 1b). This includes shallow marine vents at Mapachitos and intertidal hot springs at Mapachitos and Posada Concepcion (Fig. 2). The submarine hot springs have discharge temperatures of up to 87 °C (measured at a depth of 10 cm in the sediment), pH values between 5.9 and 6.2, and salinities between 26 and 32 g/kg (Prol-Ledesma et al. 2004). The intertidal hot springs at Mapachitos and Posada Concepcion have discharge temperatures between 60 and 72 °C, pH values of 6.2 to 6.5, and salinities of up to 27 g/kg (Villanueva-Estrada et al. 2012).

Both the submarine hot springs and the springs in the intertidal zone vent sodium-chloride waters (Prol-Ledesma et al. 2004). Compared to seawater, the liquids discharged in Mapachitos are enriched in As, B, Ba, Ca, Hg, Mn, Si, and Sr (Prol-Ledesma et al. 2004), whereas the Posada Concepcion waters show an enrichment in As, B, Ba, Ca, Fe, Li, Mn, Si, and Sr (Villanueva-Estrada et al. 2012).

Prol-Ledesma et al. (2004) calculated a reservoir temperature of about 200 °C for the hot springs of the BC. Based on oxygen and hydrogen stable isotope analyses, these authors

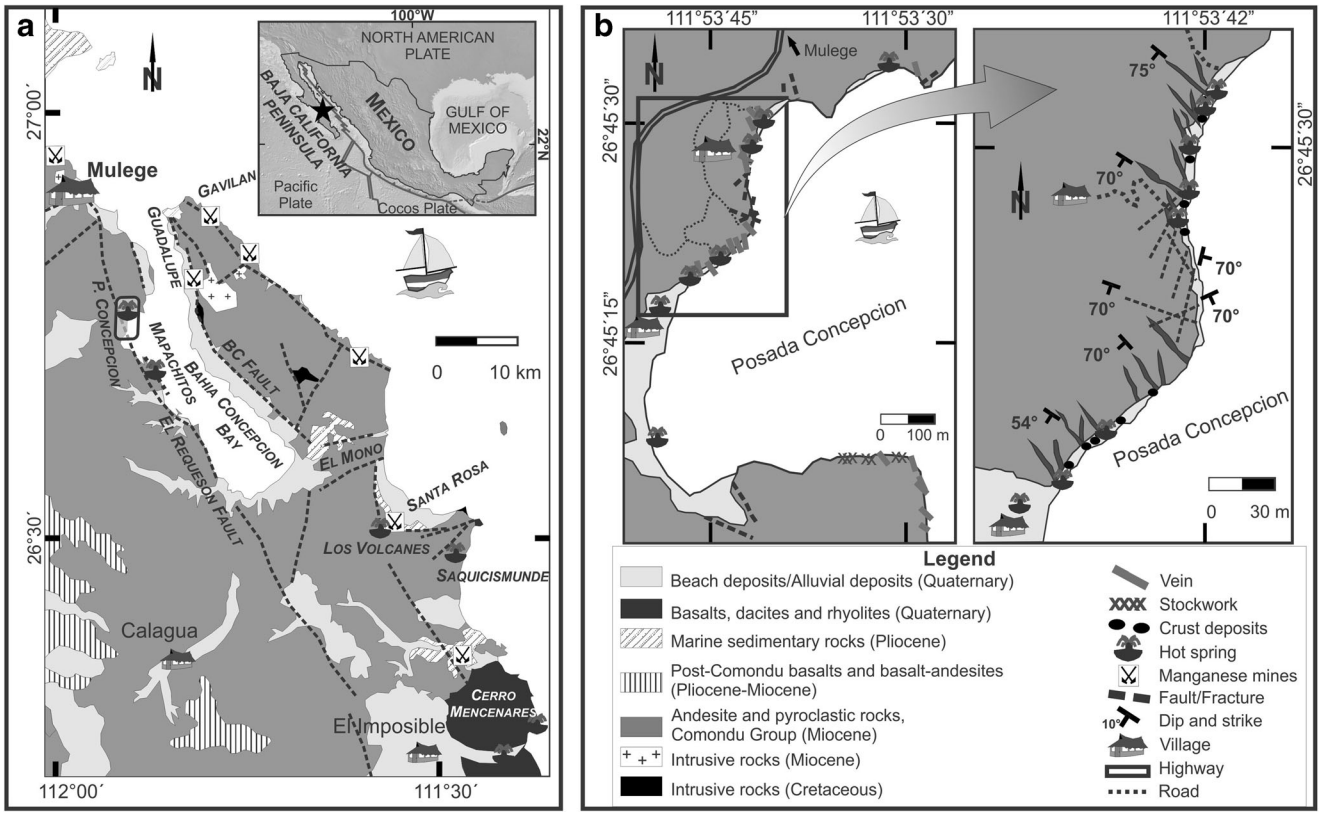

Fig. 1 Geology of the study area on the Baja California Peninsula, Mexico. **a** Geologic map of Bahia Concepcion showing the distribution of hot springs. **b** Detailed map of the coastal hot springs of Posada Concepcion

found that the hydrothermal fluids are mostly of meteoric origin. Combining geochemical modeling and fluid inclusion data, Villanueva-Estrada et al. (2012) deduced that a mixing process occurs at depth in the hydrothermal system, at a ratio of about ~ 20–30% of a high-salinity fluid with ~ 70–80% of a deep-circulated meteoric fluid. Further mixing can take place with seawater within the shallow subseafloor prior to discharge on the seafloor.

The sediments are coated with orange-yellow and greenish biofilms in areas with continuous venting and bubbling. Mapachitos hot springs are surrounded by opal crusts and opal, barite, todorokite, romanechite, ferrihydrite, pyrite, and cinnabar aggregates, as well as silica-carbonate stromatolites (Canet et al. 2005).

Methodology

Thirty samples were collected from the coastal hot springs of BC. Samples were acquired from hydrothermal deposits, altered rock, and organosedimentary stromatolites. All samples were examined by optical microscopy and analyzed by electron microscopy. A Jeol JXA-8900R electron microprobe of the *Laboratorio Universitario de Petrología* at *Instituto de Geofísica*, *Universidad Nacional Autónoma de México* (UNAM), was used to obtain back-scattered electron (BSE) images, to conduct semi-quantitative chemical analyses by energy-dispersive spectrometry (EDS) and quantitative analyses, and generate elemental maps by wavelength dispersive spectrometry (WDS). Additional imaging was conducted using a FEI Quanta 400 environmental electron microscope at the *Centro de Instrumentación Científica* of the *Universidad de Granada*, Spain.

Quantitative WDS analyses of Mn oxides were conducted using an accelerating voltage of 10 kV, a beam current of 20 nA, a spot size of 1 μm, and a counting time of 15 s, except for Pb and Ag, which had a 20 s counting time. Analyses of Ag minerals were obtained using a 20 kV acceleration voltage, 20 nA beam current, a spot size of 1 μm, and a counting time of 20 s. Plagioclase (Ca$K\alpha$), biotite (K$K\alpha$), diopside (Na$K\alpha$), rhodonite (Fe$K\alpha$), kaersutite (Si$K\alpha$), almandine (Mg$K\alpha$), kaersutite (Al$K\alpha$), sphalerite (Zn$K\alpha$), galena (Pb$M\alpha$), barite (Ba$L\alpha$), bustamite (Mn$K\alpha$), cuprite (Cu$K\alpha$), and Ag metal (Ag$L\alpha$) were used as standards for the analysis of the Mn oxides. Ag metal (Ag$L\alpha$), marcasite (S$K\alpha$), Au metal (Au$L\alpha$), cuprite (Cu$K\alpha$), bismuth selenide (Bi$M\alpha$ and Se$K\alpha$), skutterudite (Ni$K\alpha$, As$K\alpha$, *Fe*$K\alpha$), kaersutite (Si$K\alpha$ and Mn$K\alpha$), stibnite (Sb$L\alpha$), cinnabar (Hg$L\alpha$), and tellurium (Te$L\alpha$) were used as standards for the analysis of Ag minerals. The detection limits for all elements were 0.04 wt.%.

Fig. 2 Field photos of the main coastal hot spring sites and mineralization styles of the Bahia Concepcion. **a** Coastal hot springs at Mapachitos and Posada Concepcion, arrows indicate direction of discharge. **b** Symmetrical banded opal and Mn oxide veinlet. **c** Hand specimen of a colloform banded Mn oxide vein. **d** Banded opal vein cross-cutting altered andesite. **d** Opal stockwork hosted in pyroclastic rock. **e** Argillic altered pyroclastic rock adjacent to the main fault

Element X-ray mapping was conducted using the same instrument. Maps were made in a single accumulation by utilizing four WDS spectrometers simultaneously. Maps of Mn, Ca, Ba, Mg, and K in Mn oxide bands were obtained at an accelerating voltage of 15 kV and beam current of 100 nA.

The altered samples were analyzed by shortwave infrared reflectance spectroscopy (SWIR) to identify silica minerals and clay mineral assemblages, using a portable LabSpec Pro Spectrophotometer (Analytical Spectral Devices, Inc.) at the *Departamento de Recursos Naturales* of the *Instituto de Geofísica*, UNAM. Shortwave infrared spectra were collected from altered outcrops. Samples were broken in the field, such that the effect of surface weathering is minimized. Subsequent spectral measurements were conducted in the laboratory. We used spectral features of the SWIR wavelength region (1300–2500 nm). Identification of the SWIR-active minerals was made manually by comparing the wavelength position of the absorption features and the shape of the spectra (without hull subtraction) with spectral libraries and tables (Clark et al. 2007).

The bulk mineralogy of Mn deposits was established by X-ray diffraction (XRD). Measurements were made using a PHILLIPS PW 1710® diffractometer, with CuKα radiation and a graphite monochromator. The instrument was operated at 40 kV and 40 mA. X-ray diffraction patterns were obtained between 3 and 35°2θ, with a step speed of 0.05° 2θ/s and an integration time of 4 s. Mineral identification was made using

the XPowder® software and index cards PDF2 at the *Departamento de Mineralogía y Petrología* at *Universidad de Granada*, Spain. The mineralogy of silica deposits was verified by powder XRD analyses. Measurements were made using a Shimadzu XRD-6000 diffractometer operating with an accelerating voltage of 40 kV and a filament current of 30 mA, using CuKα radiation and graphite monochromator at the *Instituto de Geología*, UNAM. Bulk samples were measured over a 2θ range of 2–70° in steps of 0.02° and 2 s integration time. Data was interpreted using the Shimadzu software.

The identification of opal types was established by XRD patterns and measurements of full width at half maximum (FWHM) according to Herdianita et al. (2000). In addition, microtextural criteria were used to identify opal types (cf. Lynne et al. 2005). Mn oxides were identified based on their XRD patterns (cf. Post 1999; Dolenec 2003 and references therein).

Whole-rock major element analyses were performed by X-ray fluorescence (XRF) spectrometry on fused glass disks at the *Instituto de Geología* (UNAM), using a Siemens SRS 3000 sequential spectrometer. Details on the analytical procedures are given in Lozano and Bernal (2005). Trace elements were analyzed by inductively coupled plasma-mass spectrometry (ICP-MS) at Actlabs in Ancaster, Ontario, Canada. A correlation matrix has been obtained from the geochemical data using the software Statistica version 10. The coefficient correlations show a high significance level of $P < 0.05$ for $r > 0.65$.

Pourbaix stability diagrams were constructed using the Geochemist's WorkBench software version 9.0 to identify favorable pH and redox conditions for chemical deposition of Mn and Ag minerals in coastal hot springs. These diagrams were constructed considering activities of $10^{-4.67}$ (Ag), $10^{-2.27}$ (SO_4^{2-}), $10^{0.07}$ (Cl^-), $10^{-0.67}$ (Mn), $10^{-5.60}$ (Ba), and $10^{-2.61}$ (HCO_3^-) at a temperature of 65 °C (average temperature of thermal discharges). These activity values were calculated from concentrations analyzed in the thermal fluid by Villanueva-Estrada et al. (2012).

The most important Ag species for typical seawater were included in the stability diagram as Ag speciation depends on the Cl/Ag ratio under oxidizing conditions (Levard et al. 2012). In this study, the silver chlorine complexes were considered as the predominant Ag species.

General characteristics of Posada Concepcion hot spring deposits

Fieldwork in the BC area showed that hydrothermal mineral assemblages occur as veins and stockwork, breccias, cemented aggregates, patinas, and crusts, as well as Mn-silica-carbonate organosedimentary stromatolites (Fig. 2). These deposits are fully exposed during low tide. The host rocks include andesites, andesitic ash-lapilli tuff, sandstone, and andesitic breccias with narrow haloes of hydrothermal alteration, which are characterized by an argillic alteration assemblage of opal and clay minerals.

Veins have an average thickness of 0.5 m and extend along the strike only for a few meters (Fig. 2a–d). Stockwork structures occur locally and consist of a network of narrow (< 1 cm) veinlets (Fig. 2e). Veins show finely laminated to colloform fabrics and are composed of opal and fine-grained carbonate minerals with subordinated smectites and, occasionally, Mn oxides. Symmetrical banding is locally developed with Mn oxides enriched at vein cores (Fig. 2b, c).

Breccias occur only in a few outcrops consisting of fine- to coarse-grained clasts (up to 3 cm) of volcanic rocks containing opal within a groundmass rich in opal, carbonate minerals, and subordinate Mn oxides and barite. Cemented breccias are < 6 cm thick and occur in pavement-like deposits commonly around active hydrothermal discharge areas.

Crusts (2 m to 10 mm) and patinas (< 1 mm) extend a few meters from hot springs (Fig. 2a). They are developed as irregularly shaped patches over clasts of volcanic rocks and in the flow direction of the thermal discharge. The deposits are located on the edge of the coast and are usually covered by seawater. Patinas are composed of Mn oxides and crusts mainly consisting of Mn oxides and opal with occasional detrital fragments and bioclasts. Surfaces show bioturbation (as burrows and grazing traces) and seashell molds.

Stromatolitic organosedimentary deposits of laminated mesostructures are domal-shaped silica-carbonate deposits or Mn oxide-rich deposits with *frutexite* texture (i.e., arborescent in shape; Rodríguez-Martínez et al. 2011). Stromatolites occur adjacent to the thermal discharges.

Argillic alteration assemblage

Rocks of the Ricason Formation at Mapachitos and Posada Concepcion have been affected by argillic alteration. The argillic alteration consists of beige halos of clay minerals and opal. The alteration forms an elongated zone that extends irregularly with an NW-SE orientation from the hot springs, veins, and breccias. Field observations show that the intensity of alteration decreases laterally from the veins and breccias into the host rocks. The argillic alteration is restricted to halos a few tens of centimeters or a few meters wide on the margins of the discharge vents. In addition, irregular silicic lenses and veinlets occur within the argillic alteration zone and increase in abundance in the vicinity of the veins. The zone of alteration is characterized by calcite and Fe and Mn-oxyhydroxides veinlets. Clay minerals entirely or partially replace the plagioclase phenocrysts of the host rocks. The wall rocks typically retain their original textures.

The SWIR has been used to identify the mineralogy of argillic-altered rocks (Fig. 3). Montmorillonite is the most abundant phase in the zone of alteration at Mapachitos and Posada Concepcion. All the spectra are similar, which is consistent with the similar mineralogy in both zones. The spectra in Fig. 3a reveals absorption bands corresponding to OH^- (1400–1410 nm, with an inflection at ~1455), H_2O (1900 nm), and Al-OH, with a distinct absorption feature at 2210 nm, which is asymmetric toward longer wavelengths, a characteristic of aluminum-bearing clay minerals (e.g., Clark et al. 2007). All these features are due to OH vibrations bound to the two Al cations within the dioctahedral sheet structure of montmorillonite (Bishop et al. 2002).

Some of the samples from the alteration zone show SWIR spectra indicative of a mixture of montmorillonite with opal. The series of measurements showed that when montmorillonite is predominant (> 50 to ~ 70%), the reflectance spectra exhibited characteristics of montmorillonite and little broadening of the 2210 nm band, with a band centered at 2210–2213 nm due to the presence of opal (samples M1-Mt and M2-Mt, Fig. 3a). These findings are comparable with those of studies on mixtures of montmorillonite and opal (McKeown et al. 2011).

The spectrum of opal in the samples is characterized by the presence of OH^- and H_2O spectral features located at 1400–1410 nm, an inflection at 1455–1460 nm, majors peaks at 1900 and 1955–1960 nm, and an asymmetrical absorption center at 2205–2212 nm (Fig. 3a) due to Si-OH vibrations (Clark et al. 2007). Some of the spectra show a mixture of opal and montmorillonite. The mixture is evidenced by a band centered at about 2208–2212 nm (samples M7-Op, PC6-Op Fig. 3a), similar to that reported in mixtures with < 50% of montmorillonite (McKeown et al. 2011).

Mineralogy and chemical composition of hydrothermal precipitates

The hydrothermal precipitates of BC are composed of opal (A and A/CT), quartz, aragonite, calcite (high-Mg and low-Mg), barite, todorokite, romanechite, pyrite, acanthite, native silver,

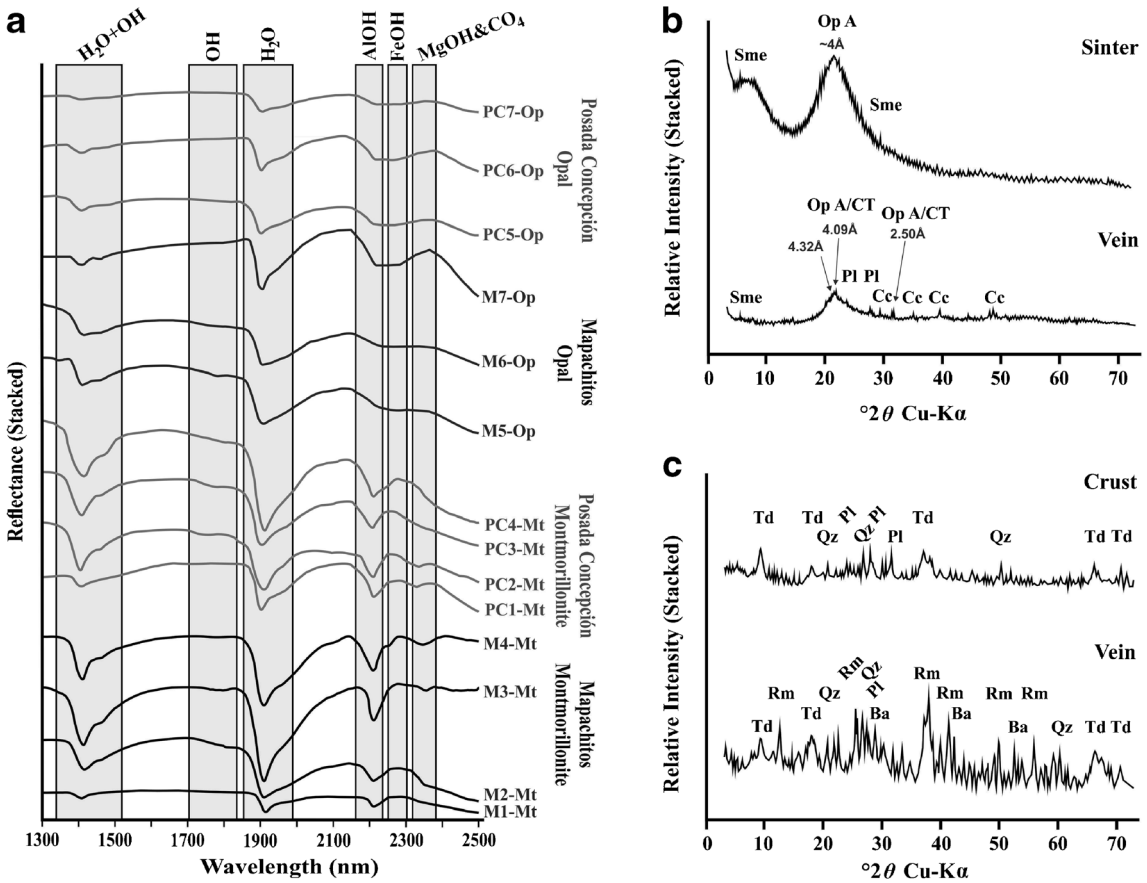

Fig. 3 Mineralogy of hot spring deposits in the Bahia Concepcion. **a** Short wave infrared reflectance spectra representative of the main alteration assemblages found at Mapachitos and Posada Concepcion. The main absorption wavelengths are marked as gray bars (Clark et al. 2007). **b** Representative X-ray diffraction profiles of sinter and opal veins. Cc, calcite; OpA, opal A; Op A/CT, opal A/CT; Pl, plagioclase; and Sme, smectite. **c** X-ray diffraction diagrams of the Mn oxides forming crusts and veins: Ba, barite; Pl, plagioclase; Qz, quartz; Rm, romanechite; Td, todorokite

montmorillonite, and grains inherited from host rock (plagioclase, augite, hornblende, and titanomagnetite).

Hydrothermal activity in Posada Concepcion resulted in three mineralization stages, as evidenced by field and petrographic observations. This includes (1) cryptocrystalline quartz, clay minerals, carbonates, and pyrite; (2) carbonates, non-crystalline silica, Mn oxides, barite, and clay minerals; and (3) quartz, non-crystalline silica, Mn oxides, carbonates, barite, silver minerals, and pyrite.

Non-metallic minerals

Opal is the main constituent of all hot spring deposits, except in crusts. Opal displays a variety of microscopic textures, including massive, colloform, crenulated, fluidal, pseudoradial and spheroidal. It occurs as veinlets and pore infills (Fig. 4a, b). Opal aggregates are rarely cut by thin veinlets (< 30 μm) of fibrous, radial, and fine polysynthetic *twining* cryptocrystalline quartz with spherulitic to tabular habits.

X-ray diffraction patterns indicate that opal corresponds to the type A for sinter deposits and stromatolites structures, and to the type A/CT for veins and breccias (Fig. 3b). Opal A forms distinctive botryoidal aggregates of microspheres (Fig. 4a) and opal A/CT forms clusters of microspheres and platy structures. In addition, Blanco-Florido (2010) reports the occurrence of filaments and tube-like microstructures, possibly of organic origin, in the deposits from Mapachitos and Posada Concepcion.

Clay minerals in the silica deposits were mostly derived from the alteration of volcanic host rocks. The dominant clay mineral is smectite, as confirmed by XRD (Fig. 3b). Based on EDS and SWIR data, montmorillonite is the most common smectite (Fig. 3a).

Carbonate minerals (high-Mg and low-Mg calcites and aragonite) are the most common precipitates after opal (Fig. 4b). Calcite was also identified by X-ray diffraction (Fig. 3a). Energy- dispersive spectrometry analyses show the presence of high-Mg calcite and low-Mg calcite. These form fine laminae, fibrous crystals of mainly aragonite and high-Mg calcite, and aggregates of bladed grains (up to 50 μm in length). Veinlets of low-Mg calcite cross-cut the opal groundmass. Barite occurs as disseminated particles within veins, crusts, and cemented aggregates, but appears as blades spheroidal aggregates or tabular crystals (< 80 μm), generally associated with Mn oxides (Fig. 4d).

Mn oxides

The Mn phases todorokite and romanechite were identified. Optically, todorokite shows low reflectivity and displays a gray to bluish hue birefringence. Todorokite occurs as finely laminated botryoidal, colloform, and folded aggregates (Fig. 4c). Radial and fan-like, as well as zoning textures, can be observed. Todorokite also forms the cement that binds the clasts and bioclasts in the Mn deposits. Romanechite has medium reflectivity, displays a grayish white color with a bluish tint, and is harder than todorokite. Romanechite occasionally occurs as irregular masses, *botryoides*, and acicular aggregates (Fig. 4c).

The XRD analyses indicate that the main component of Mn deposits is poorly crystallized todorokite (Fig. 3c). However, veins and breccias are mostly composed of romanechite. Barite is associated with the Mn oxides. In addition, XRD patterns indicate the presence of trace amounts of quartz and plagioclase (Fig. 3c).

Elemental mapping of Mn oxide crusts shows an alternation of laminae with variable Mn, Ba, Ca, Mg, and K contents, allowing the differentiation of Ba-rich and Ba-poor phases can be differentiated (Fig. 5). The Ba-rich phase is irregularly distributed but clearly replaces the Ba-poor phase (Fig. 5). Energy-dispersive spectrometry and WDS analyses have confirmed that todorokite is the Ba-poor phase and romanechite the Ba-rich phase.

The todorokite has relatively high MgO (< 5.8 wt.%), SiO_2 (< 5.1 wt.%), Na_2O (< 2.6 wt.%), K_2O (< 1 .3 wt.%), and BaO (< 1.6 wt.%) contents. Todorokite records the highest Mg, Na, and Si contents in Mn oxide-rich and stromatolitic organosedimentary deposits (ESM, Appendix 1). Wavelength dispersion quantitative analyses indicate an average structural formula of $(Na, Ca, K, Ba, Cu)_{0.7}$ $(Mn^{4+}, Mg, Si, Al, Fe)_{5.9} \cdot 2.9(H_2O)$ ($n = 10$, ESM, Appendix 1).

Romanechite is distinguished under the SEM due to its high Ba content, in contrast to todorokite (Fig. 5). Romanechite shows moderate concentrations of Ba (< 14.7 wt.% BaO) with notable amounts of Ca (~ 0.9 wt.% of CaO), Na (~ 1.1 wt.% of Na_2O), K (~ 0.7 wt.% of K_2O), Si (~ 0.4 wt.% of SiO_2), and Cu (~ 0.5 wt.% of CuO) (ESM, Appendix 1). The calculated average structural formula of romanechite is $[Ba, Na, K, Ca, (H_2O)]_{2.0}$ $(Mn^{4+}, Cu, Si, Mg, Al, Fe)_{4.6}O_{10}$ ($n = 3$, ESM, Appendix 1).

Silver minerals

Acanthite and native silver, associated with pyrite, were identified by SEM-EDS (Fig. 6). Acanthite and native silver occur as disseminated, small grains (2 to 30 μm) in veins and breccias, and in the opal-rich and Mn oxide-rich deposits formed around active hydrothermal discharges (Fig. 6). Acanthite forms aggregates of platy subhedral crystals arranged in arborescent patterns, usually filling pores (Fig. 6b). Wavelength dispersive quantitative analyses show that acanthite contains ~ 2 wt.% Fe and ~ 1 wt.% Cu. The average structural formula is $(Ag, Fe, Cu, Mn)_{2.0}$ S ($n = 3$, ESM, Appendix 2). Native silver is less abundant than acanthite and occurs as submicroscopic anhedral grains filling pores. Native silver contains significant amounts of S (< 2.1 wt.%) and Fe(< 0.9 wt.%)

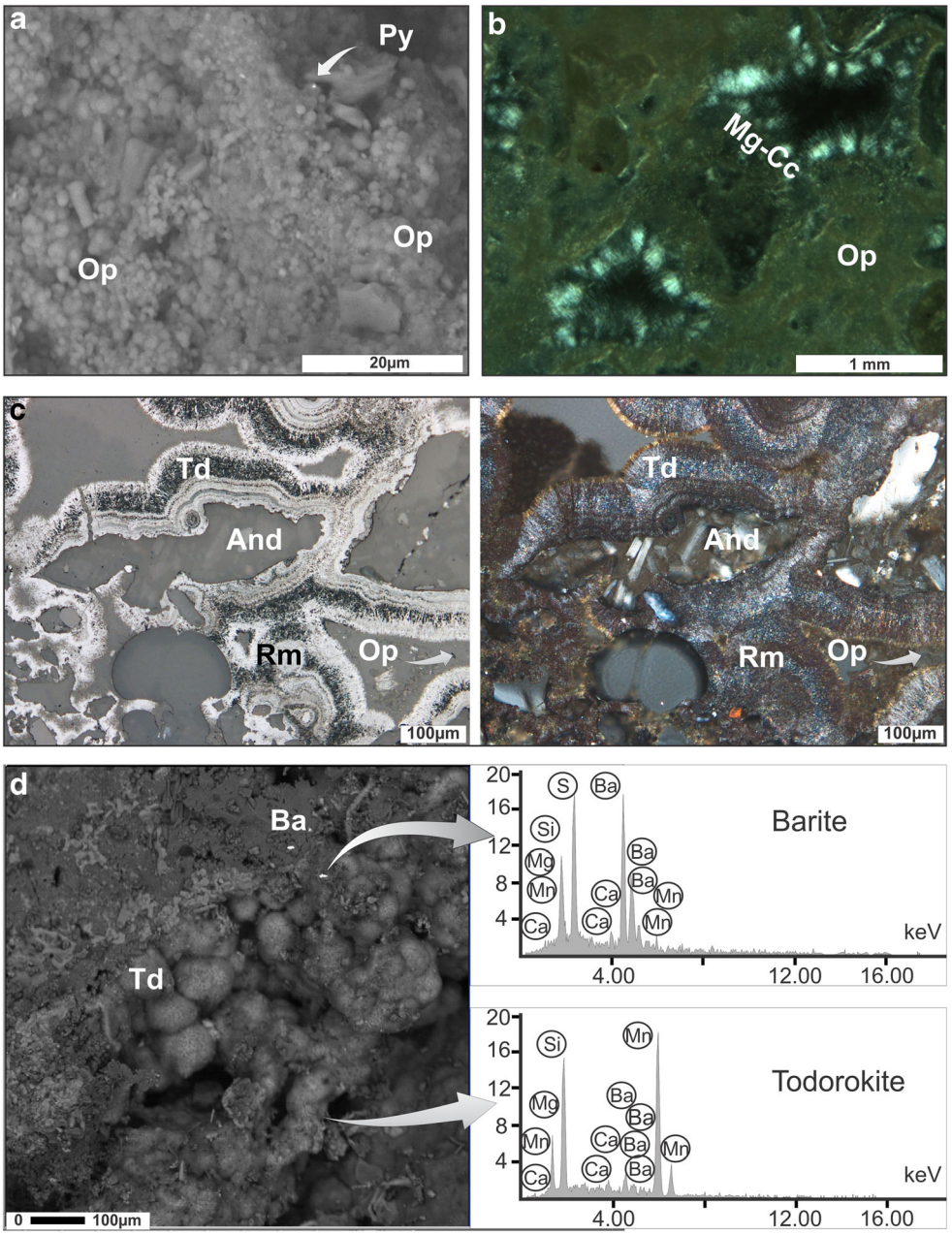

Fig. 4 Textural relationships in hot spring deposits at Posada Concepcion. **a** Scanning electron microscope image of clusters of opal-A/CT microspheres (Op) with disseminated pyrite (Py). **b** Transmitted light image showing an association of opal bands and Mg-calcite (Mg-Cc) radial aggregates within pores. **c** Reflected light (left) and crossed polarized light image (right) showing aggregate structure, Mn oxides and opal cemented volcanic clast (And), colloform bands of romanechite (Rm), todorokite (Td) and opal (Op). **d** Scanning electron microscope image of Mn oxides crust with botryoidal aggregates of todorokite associated with barite (Ba). The graphs shown on the right represent energy-dispersive spectroscopy analyses presenting the mineral composition

(ESM, Appendix 2). Pyrite forms fine-grained aggregates of subhedral grains (< 50 μm) that are disseminated within opal and Mn oxides.

Stromatolitic deposits and other structures

Adjacent to the thermal discharges and at the margins of the thermal discharge channels, a series of discontinuous and microdigitate (i.e., the radial texture of growth forming botryoidal layers; Bartley et al. 2000) organosedimentary stromatolites occur. The silica-carbonate and Mn oxide-rich stromatolitic fascicle form irregular and thick crusts growing on volcanic clasts as substrates.

Silica-carbonate stromatolites have a domal structure and variable convexity (Fig. 7a). The stromatolites exhibit laminations mainly composed of micritic and sparry Mg-rich calcite (with < 9 wt.% Mg) alternating with opal and todorokite (ESM, Appendix 1), both occurring as irregular and discontinuous lamellae. The porosity is filled by opal, with occasional calcite replacement.

Three types of microstructures of different complexity at the millimeter scale can be recognized in Mn oxide-rich stromatolites. This includes a flat-laminated stratiform microstructure of alternating layers, a thrombolitic structure (i.e.,

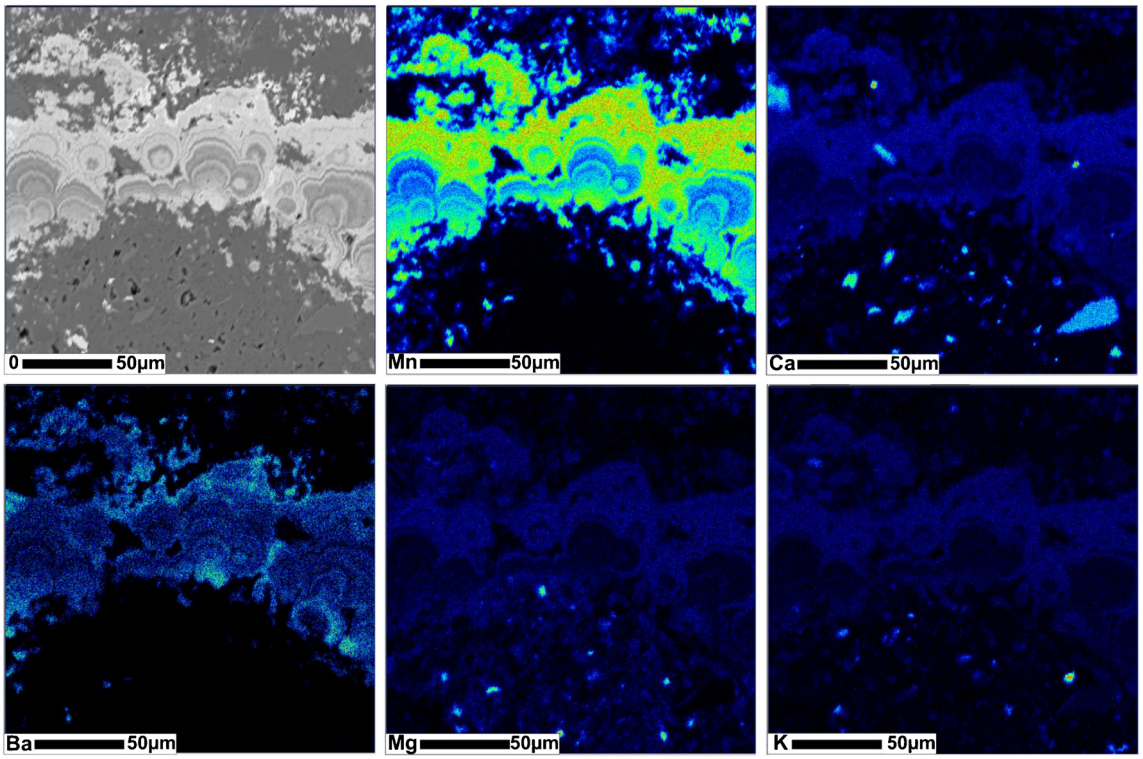

Fig. 5 Elemental maps showing the distribution of Mn, Ca, Ba, Mg, and K in the botryoidal bands on volcanic clast. The Ba is concentrated in romanechite bands that alternate with todorokite bands

without laminar lamination, irregularly shaped, adhered or not to the substrate; Riding 2011) composed of an arborescent zone and a poorly laminated zone with terete growth (Fig. 7b), and a well-developed microdigitate fabric, with growth in a dendritic shape formed by divergently branched microcolumns, similar to *frutexites* texture (Fig. 7c).

Cemented aggregates, crusts, and patinas of Mn oxides show organic structures. Todorokite replaces bioclasts and covers organic debris, creating a cast of organic structures resembling tube worms (Fig. 7d). In addition, there are recent trails probably made by organisms moving along the surface of an unconsolidated Mn deposit, similar to *pascichnia* structures (Fig. 7e).

Associated with continuous venting and bubbling, there are orange-yellow and green biofilms partially covering the sediments. The biofilms are < 5 mm thick and show beige-green bands. Only scattered, gray, dried remains of former biofilms occur in local depressions.

Geochemistry of hot spring deposits

A suite of 16 samples was collected from the mineralized zones representing different hot spring deposits of the BC. We also used geochemical data of coastal hot spring deposits from Mapachitos reported by Canet et al. (2005). Results of major and minor elements in hot spring deposits are given in ESM, Appendixes 3 and 4, respectively. These deposits show large differences with respect to their SiO_2 and MnO contents (ESM, Appendix 3). Mineralized rocks are divided into two distinct types based on their mineralogical and chemical composition. Box-and-whisker plots illustrate characteristics of geochemical data distributions, such as the spread of data, median, and upper and lower quartiles. They also summarize the relationship of higher concentrations of minor and trace elements for each of the groups (Fig. 8).

The first group consists of silica-rich deposits containing opal and quartz. The median value for SiO_2 is about 70 wt.% ($n = 11$), with significant concentrations of CaO (median value 1.3 wt.%, $n = 11$) and MgO (median value 0.4 wt.%, $n = 9$). The $Fe_2O_{3(t)}$ and MnO concentrations are less than 3 wt.% (Fig. 8). The samples have a high SiO_2/Al_2O_3 ratio with an average of 83.0 ($n = 12$) and a high Fe/Mn ratio with an average of 35.0 ($n = 12$). The second group of samples was taken from Mn oxide-rich deposits with MnO contents ranging from 8.28 to 48.18 wt.% (median value 36 wt.%, $n = 11$). The high MnO concentration recorded are higher than the values of silica-rich deposits (<1 wt.%, Fig. 8). The SiO_2 content is relatively low (median value 36 wt.%, $n = 11$) compared to the median value of the first group. In these Mn-rich samples, the median values for CaO (8.8 wt.%) and MgO (4.7 wt.%) are higher the corresponding values of silica-rich deposits (Fig. 8). The average SiO_2/Al_2O_3 ratio in the Mn oxide-rich samples is 5.94 ($n = 11$). Manganese oxide-rich samples are relatively low in Fe, with average Fe/Mn ratios of 0.27 ($n = 3$) (ESM, Appendix 3).

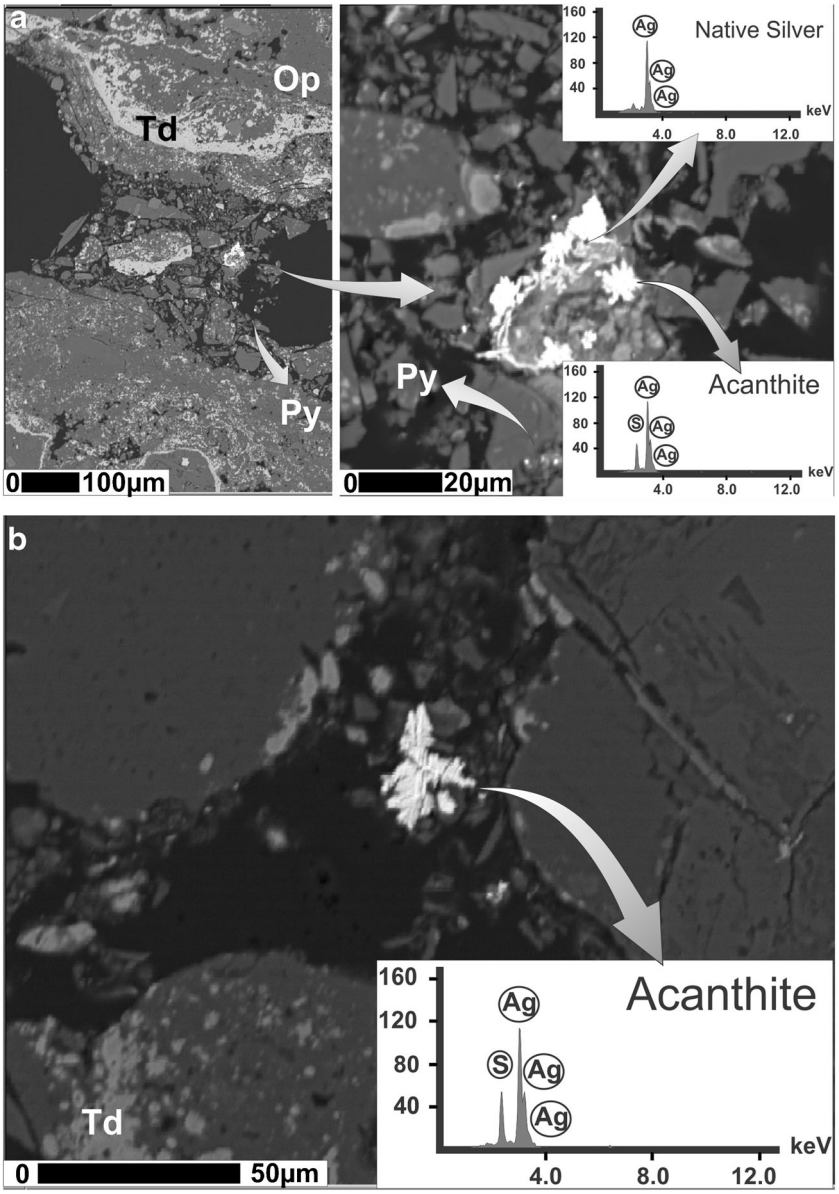

Fig. 6 Scanning electron microscope (backscattered electron) images and energy-dispersive spectroscopy analyses showing native silver and acanthite in vein-breccia from coastal hot springs. **a** Association of silver minerals, opal (Op), pyrite (Py), and todorokite (Td). **b** Crystal aggregates of acanthite associated with todorokite occurring in the matrix

The trace element results given in ESM, Appendix 4 reveal that both groups of samples are distinctly enriched in As (< 5112 ppm), Ba (< 30 wt.%), Cu (< 340 ppm), Pb (< 34 ppm), Sb (< 189 ppm), Sr (< 6990 ppm), Tl (< 7 ppm), V (< 399 ppm), W (< 964 ppm), and Zn (< 310 ppm). There is a considerable overlap between the concentrations ranges of As, Ba, Pb, Sb, Sr, W, and Zn, but there is a tendency toward somewhat lower values within the group of silica-rich deposits (Fig. 8). Deposits rich in Mn show the highest enrichment in Cu, V, and Tl. Barium is distinguished by its wide variability in deposits rich in silica.

The inter-element relationships in the studied coastal hot spring deposits are listed in ESM, Appendix 5. Correlation matrices have been calculated for two sample sets. The silica-rich deposits have a common positive correlation among Ca with As ($r = 0.94$), Co with Pb ($r = 0.94$), Mo with Tl ($r = 0.99$), Sr with Ba ($r = 0.99$), and Zn with Ba ($r = 0.96$) and Sr ($r = 0.94$). In addition, As, Ba, Cu, Mn, Mo, Pb, Sb, Sr, Tl, U, V, and Zn are fairly well grouped (ESM, Appendix 5). The Mn oxide phase-rich deposits exhibit a positive correlation between Ag and U ($r = 0.98$), Cu and Sr ($r = 0.90$), and Sb and Pb ($r = 0.88$). Likewise, Ag, As, Ba, Cu, Ni, Pb, Sb, Sr, Tl, U, and V show a positive correlation (ESM, Appendix 5).

Discussion

Classification of Mn-Ag mineralization

The BC is host to several Mn-Ag mineralizations formed since the middle Miocene (Fig. 1). The largest and economically

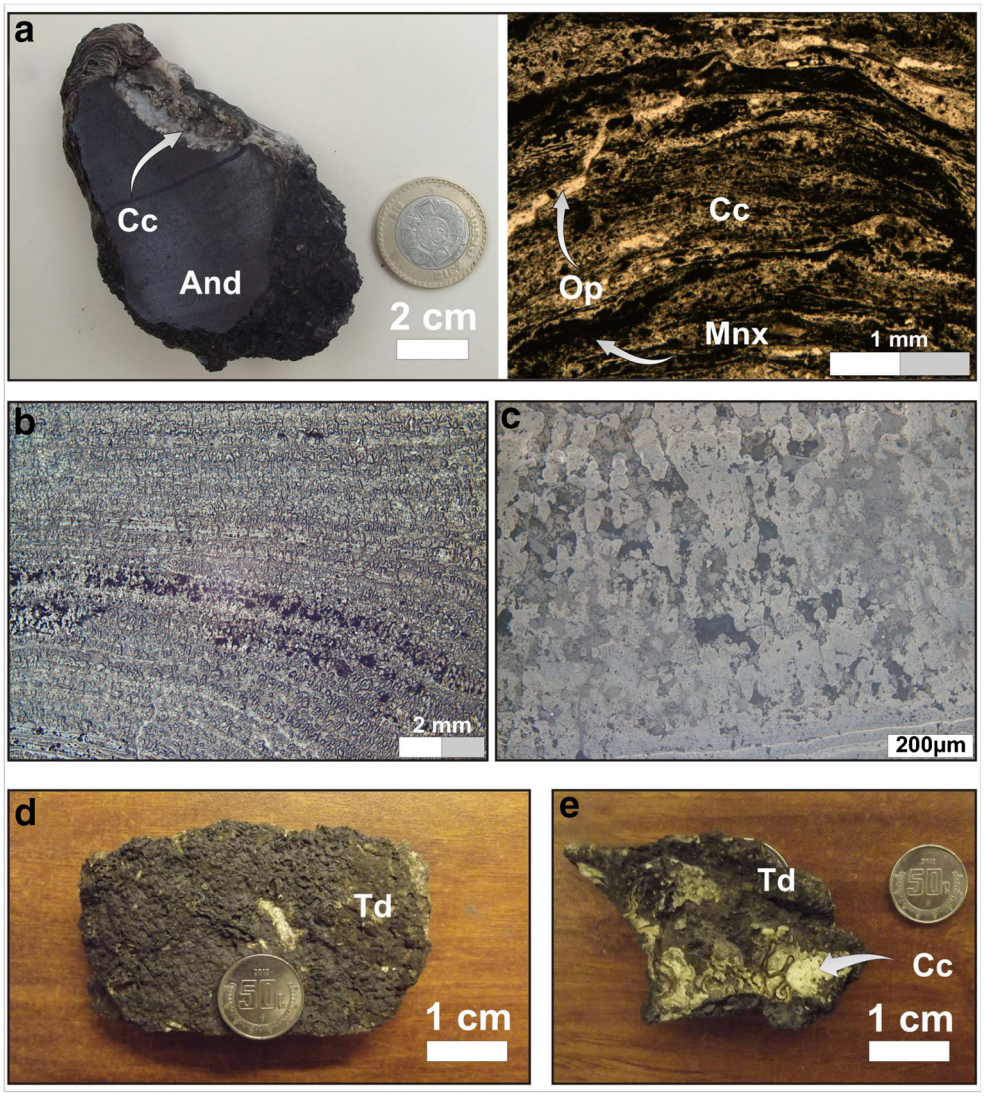

Fig. 7 Hand specimens of apparent organic activity in the coastal hot springs at Posada Concepcion. **a** Silica-carbonate stromatolite structure on andesite (And), calcite (Cc). At the right hand of the figure, there is a microphotograph of fine-layered carbonate stromatolite, associated with Mn oxides (Mnx) and opal (Op). **b** Thin section of Mn oxides stromatolites with a thrombolitic structure. **c** Detail of colloform laminae and arborescent development of todorokite, shown in reflected light. **d** Appearance of worm molds of Mn oxides, todorokite (Td). **e** Worm tracks on Mn oxides crust

most important ore deposit are middle to late Miocene El Gavilan, late Miocene Guadalupe, and Pliocene Santa Rosa (Camprubí et al. 2008; Rodríguez-Díaz et al. 2010). The Mn deposits occur as NW-SE veins and breccias, and are composed by Mn oxides (ramsdellite, pyrolusite, romanechite, todorokite and coronadite), barite, base metal sulfides, calcite, dolomite, opal, and quartz. Ore grades ranges up to 36% Mn and 64 g/t Ag (Terán-Ortega et al. 1993; Rodríguez-Díaz et al. 2008).

The area of BC has recorded hydrothermal activity during the late Miocene occurred until recently in response to the extension associated with the Miocene Gulf of California opening (Camprubí et al. 2008). The extensional tectonic settings results in a high heat flow, with the basin-bounding, and strike-slip faults providing major fluid pathways allowing the development of convective hydrothermal systems (Lachenbruch et al. 1985).

The hydrothermal activity at Posada Concepcion and Mapachitos is manifested by subaerial and shallow-submarine hot springs. The same NW-SE fault system within the BC basin and the mineralogical similarities suggests that Mn-Ag deposits around the hot spring sites could be an active analog for mineralization processes that generated hydrothermal Mn deposits (El Gavilan, Guadalupe, and Santa Rosa deposits) from the Miocene to the Pliocene. Berger and Eimon (1983) and Kilias et al. (2001) suggested a similar connection between hot spring type and open vein type mineralizations, possibly forming a continuum from surface precipitates to deep veins.

The occurrence of the mineral assemblage of todorokite, romanechite, non-crystalline silica, barite, pyrite, acanthite and native silver in coastal hot springs of the BC area is comparable to other shallow submarine deposits such as those of western Milos in Greece (Liakopoulos et al. 2001; Alfieris et al. 2013; Papavassiliou et al. 2017), and related to a possible vertical mineral zoning with a higher concentration of sulphide mineralization at depth (e.g. different styles of epithermal-hot spring deposits Bastin 1948; Hewett 1968;

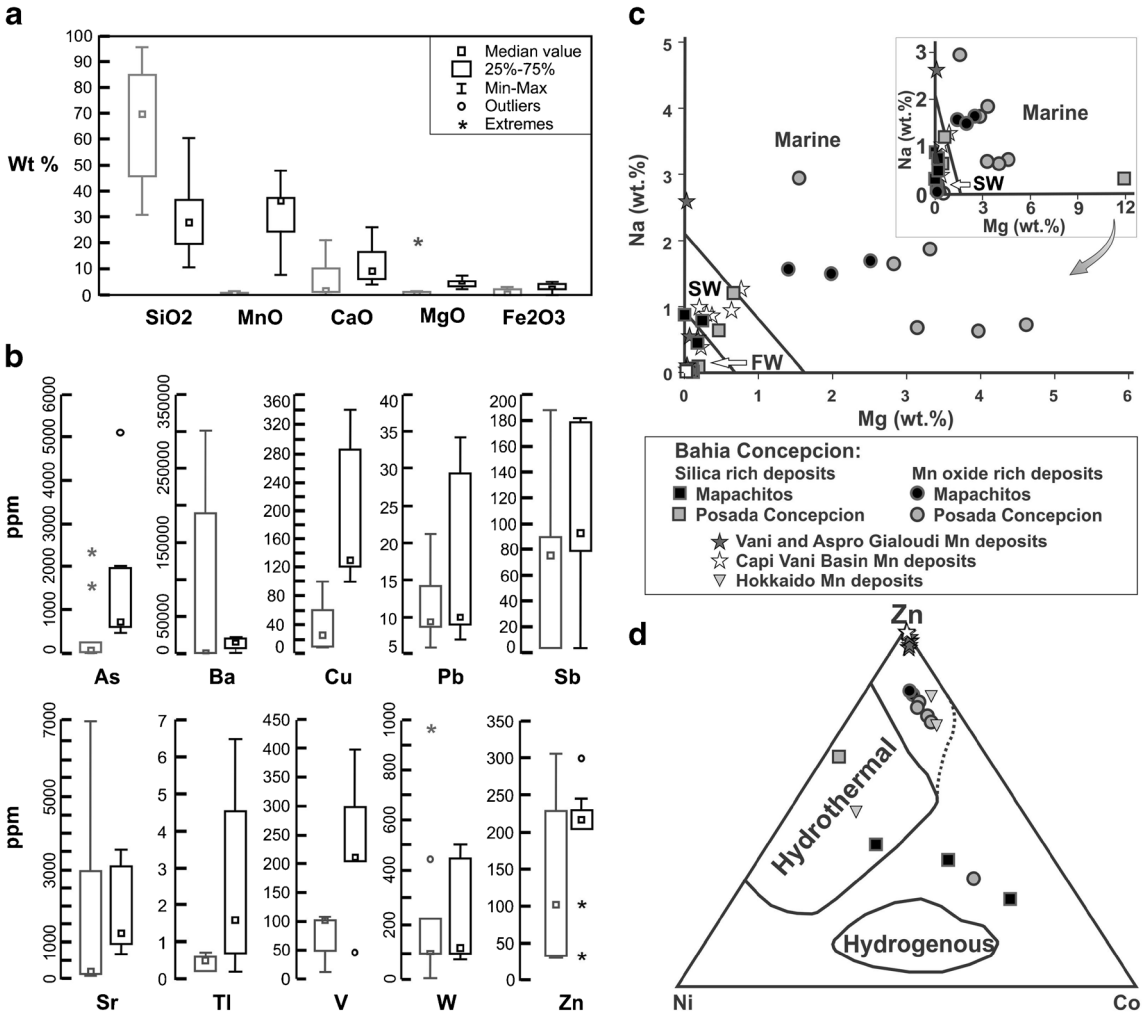

Fig. 8 Geochemistry of hot spring deposits in the Bahia Concepcion. **a** Box-and-whisker plots of major elements. Data have been separated into two groups: silica-rich (gray boxes, $n = 11$) and Mn oxide-rich deposits (black boxes, $n = 9$). The boxes enclose the interquartile range (25th and 75th percentile) with the medians displayed as squares. The whiskers extend from the upper and lower hinges to the maximum and minimum values. Separate points indicate unusual values that occur far from the bulk of the data. **b** Box-and-whisker plots of trace elements show comparable data ranges between both groups of deposits. **c** Discrimination diagram from different Mn settings (Nicholson 1992). The samples of shallow marine hot spring deposits share the shallow and fresh water fields. Fresh water (FW) and shallow marine water (SW). **d** Co-Ni-Zn ternary diagram showing fields of hydrothermal and hydrogenous deposits (Choi and Hariya 1992). The dotted line represents the extension of the hydrothermal field for samples with enrichment in Zn of continental and shallow water hot springs deposits. For comparison, hot spring Mn deposits have also been plotted. Continental deposits are from Hokkaido, Japan (Miura and Hariya 1997), and shallow marine deposits are from Vani (Hein et al. 2000), and Vani and Gialoudi Milos Island, Greece (Papavassiliou et al. 2017)

Sillitoe 1975; Berger and Eimon 1983; Crespo and Lunar 1997; Leal et al. 2008; Gómez-Caballero et al. 2010).

Mineral assemblage and geochemical signatures

The Mn oxides of the BC consist of poorly crystalline phases (Fig. 3) and show significant enrichments in Ba, Si, Mg, Ca, Na, and Cu (ESM, Appendix 1). These characteristics can be explained by the interaction of mineralizing solutions and seawater, which produce abrupt changes in pH and redox conditions (Ostwald 1982; Nicholson 1992; Lugović et al. 2008) that may affect the adsorption mechanism of transition metals by the oxides of Mn (Post 1999; Sinisi et al. 2012). The enrichment and variation of Ba in the Mn oxides (Fig. 5) are interpreted by pulses of hydrothermal fluid with the variation of the input of Ba and changes in fluid temperature that determine the precipitation of Ba-Mn oxides or the incorporation of the Ba to a Mn oxide poorly crystalline phase (Granina et al. 2007).

The Mn oxides are enriched in MgO (< 5.8 wt.%). The high MgO content can be attributed to (a) the deposition in the shallow marine environment by the hydrothermal fluids, which are oxidizing in character and have a near-neutral pH (Nicholson 1992) and (b) a biogenic contribution to the marine environment (Dolenec 2003; Lugović et al. 2008). The

Mg/Mn ratio of the stromatolitic todorokite samples varies from 0.07 to 0.08 (ESM, Appendix 1). These values suggest that the chemical species of manganates (Mn^{4+}, 10 Å todorokite) are of microbial origin (Mandernack et al. 1995). The influence of microbial mediation processes for mineral precipitation, especially Mn oxides, has been documented by several authors (Usui and Mita 1995; Mita and Miura 2003; Tebo et al. 2004). This is consistent with textural observations and mineral chemistry of stromatolites. In addition, the presence of orange-yellow and green biofilms over the sediments around thermal venting suggests recent microbial activity. This evidence suggests that the Mn oxides in Posada Concepcion were influenced by bio-chemogenic processes.

The silica deposits consist of opal associated with quartz, calcite, aragonite, pyrite, barite and Mn oxides. The structure and laminated texture of the non-crystalline silica (Opal A and Opal A/CT) deposits constitute sinters around the thermal discharges. Opal is a common component of sinters related to subaerial hot springs (Herdianita et al. 2000). In hot spring environments silica precipitates from near-neutral and alkaline sodium-chloride waters (Lynne et al. 2005). In addition, silica precipitation is mediated by microbial activity (Jones et al. 2001). For example, microbial silicification with deposition of sulfides containing Au and Ag at the subaerial Champagne Pool hot spring in the Waiotapu geothermal field, New Zealand (Jones et al. 2001). The occurrence of organosedimentary stromatolites and filamentous tubular remnants within the non-crystalline silica deposits (Blanco-Florido 2010) record former microbial activity associated with the coastal hot springs at Posada Concepcion. The occurrence of banded veins with sulfides, sulfates, and oxides minerals together with stromatolites and maturation of the silica phases from opal A to opal A/CT (cf. Herdianita et al. 2000; Lynne et al. 2005) suggests that the hydrothermal activity of coastal hot springs was ongoing for some time.

The deposits of BC exhibit significant variations in their SiO_2 and MnO contents as they are either rich in opal or Mn oxides. Silica and Mn-rich deposits in Mapachitos and Posada Concepcion are characterized by high and low Fe/Mn ratios, respectively (ESM, Appendix 3). It is considered that the fractionation between Fe and Mn took place during their formation in the coastal hot springs, similar to exhalative manganiferous sediments ($0.1 > Fe/Mn > 10$, Nicholson 1992), and comparable to ratios < 1 characteristic of lacustrine deposits (Nicholson 1992). The fractionation between Fe and Mn is related to the differences in their solubilities, with an initial precipitation of Fe-bearing minerals followed by another of Mn-bearing phase (Toth 1980).

The hot spring Mn deposits show an enrichment in SiO_2, CaO, MgO, and Ba (ESM, Appendixes 3 and 4). The Mn deposits of hydrothermal origin generally have an enrichment in Si (Choi and Hariya 1992). In the silica-rich deposits of BC values exceeding 90% SiO_2 are reached (Fig. 8). High SiO_2/Al_2O_3 ratios of silica-rich deposits show a clear hydrothermal affinity (83.02, Choi and Hariya 1992), while in deposits rich in Mn phases, there is a considerable detrital contribution (SiO_2/Al_2O_3 ratio avg.: 5.92 and Si-Al positive correlation $r = 0.74$). In the latter case, the geochemical signature is related to the mixing of the hydrothermal precipitates with coastal detrital sediments (e.g., breccia observed with petrography.).

A high content of MgO in the hydrothermal deposits is an indicator of a contribution of marine water to the mineralizing fluids (hydrothermal fluid of meteoric source, Prol-Ledesma et al. 2004), especially in the formation process of Mn oxides (Fig. 8c, Nicholson 1992). There is a clear relation between hydrothermal fluids and seawater in shallow marine springs that favors the deposition of Mn (Hein et al. 2000; Papavassiliou et al. 2017). Manganese precipitates may also scavenge MgO and other trace elements in direct proportion to their concentration in seawater (Nicholson 1992). Additionally, the incorporation of Mg in calcite is favored in hydrothermal environments (Montes-Hernandez et al. 2016).

Enrichment of Ba is attributed to the presence of barite and Ba-rich Mn oxides in the deposits of the coastal hot springs. The precipitation of barite can occur due to mixing of Ba-rich hydrothermal fluid with sulfate-rich seawater. The significant enrichment of Ba may be due to the leaching process caused by alteration of hydrothermal fluids to the feldspars of granitic basement or the basaltic-andesitic rocks of the Comondu Group. Barite has been reported frequently from modern submarine and subaerial hot springs (Binns et al. 1997; Hein et al. 2005; Kanellopoulos et al. 2017).

The strong positive correlations between silica-rich and Mn oxide phase-rich deposits imply that these elements are enriched as a result of a similar geochemical behavior (Fig. 8, ESM, Appendix 5). The deposits of BC show a correlation between Ag, As, Ba, Ca, Cu, Mg, Pb, Sb, Sr, Tl, and Zn (ESM, Appendix 5). This geochemical signature is consistent with a Mn-Ag-As-Ba-Cu-Pb-Sb-Sr-Tl-V-W-Zn association in Mn oxides deposited by hydrothermal processes in continental (Hewett 1968; Nicholson 1992; Usui and Mita 1995), shallow (Hein et al. 2000; Liakopoulos et al. 2001; Alfieris et al. 2013) and submarine environments (Hein et al. 2005). This association of elements can be considered as diagnostic for hydrothermal Mn deposits and serves as a guide in the exploration of shallow marine hydrothermal deposits (Alldrick 1995).

The use of geochemistry to aid in the identification of hydrothermal Mn mineralization was described by several authors (Choi and Hariya 1992; Nicholson 1992). The ternary Ni-Zn-Co diagram (Fig. 8d, Choi and Hariya 1992) shows interpreted hydrothermal fields for BC deposits and continental (Miura and Hariya 1997) and shallow marine hot springs (Hein et al. 2000; Papavassiliou et al. 2017). Discriminations diagrams for BC deposits show a trend toward the areas of the extreme members

of Co and Zn, and a slight enrichment in Co and Ni (ESM, Appendix 4) falling outside the hydrothermal fields (Fig. 8d).

The crystal structure of todorokite has space to hold large amounts of trace element, especially Co and Ni (Post 1999), such as at Posada Concepcion (Fig. 3c). The slight enrichment is comparable with those observed in the shallow marine hydrothermal system of Milos (Papavassiliou et al. 2017), the Boleo Cu-Co-Zn deposit of the Baja California Peninsula (Conly et al. 2011), and lacustrine hot spring deposits in central Spain (Crespo and Lunar 1997). The deposits of BC, shallow marine hot springs from Vani and Aspro Gialoudi, Greece (Hein et al. 2000; Papavassiliou et al. 2017), and continental hot spring from Hokkaido, Japan (Miura and Hariya 1997) in the Ni-Zn-Co diagram (Choi and Hariya 1992) are distributed in an area adjacent to the hydrothermal field, suggesting that a slight extension of the hydrothermal field toward the Zn end member may be needed in this classification diagram.

Genetic model

Formation of the Mn-Ag mineralization in the extensional BC basin involves convective circulation of hot solutions (reservoir temperature 200 °C, Prol-Ledesma et al. 2004) and the interaction of these fluids with the granitic basement and the rocks of the Comondu Group (Fig. 9). The fluid-rock interaction resulted in an enrichment of Mn, Ca, Ba, Si, and Ag in the hot solutions and the deposits formed from them. This is consistent with isotopic Pb, Os, and Sr data from the Boleo and Lucifer Mn deposits that indicate the interaction of mineralizing fluids with the granite basement, volcanic rocks of the Comondu Group and a sedimentary unit for the mineralization for the origin of metals (del Rio-Salas et al. 2008; Conly et al. 2011).

At depth, a mixing process occurs between a meteoric hydrothermal fluid and saline fluids (11%wt. NaCl eq., Villanueva-Estrada et al. 2012). High-chloride concentrations are required for the low temperature (< 250 °C) hydrothermal solutions to effectively leach and transport Mn and Ag

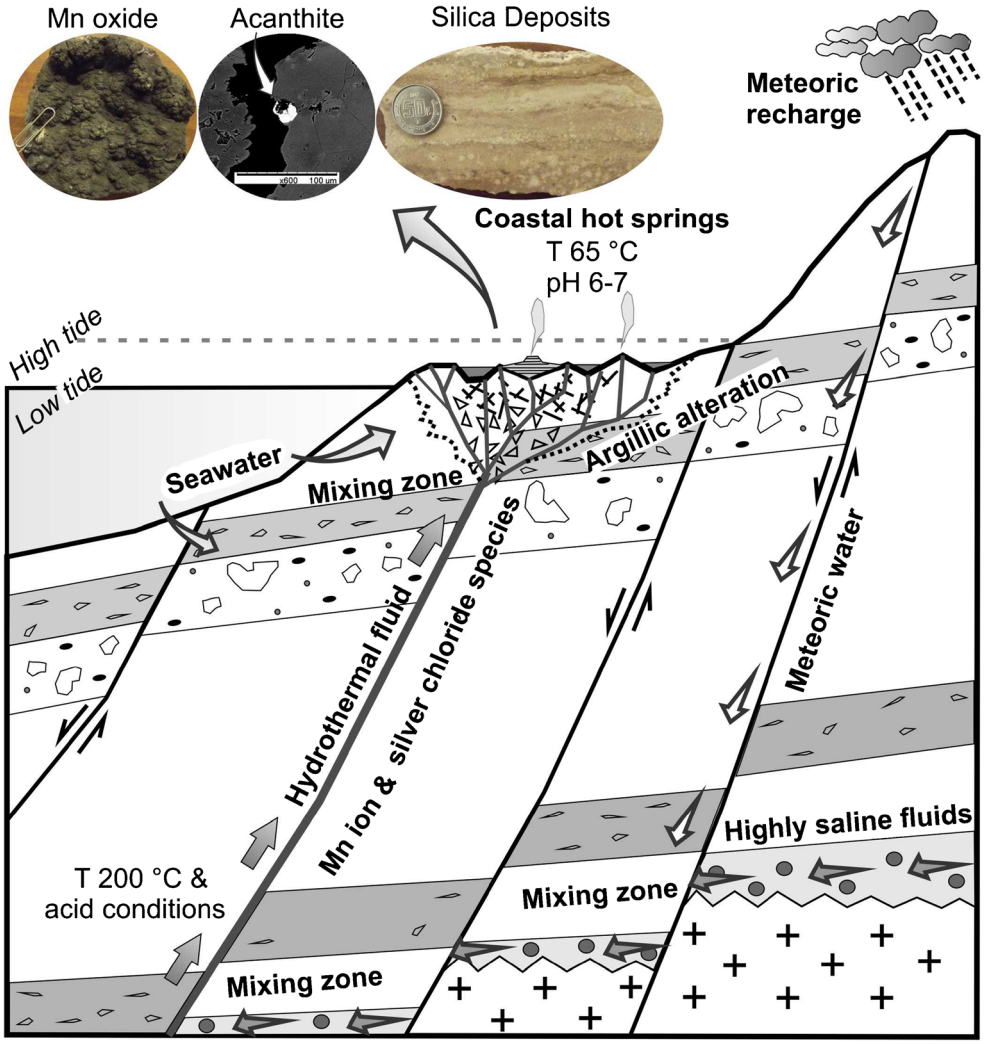

Fig. 9 Schematic model for the convection-dominated hydrothermal system of the Bahia Concepcion. The flow path considered in the geochemical modeling includes meteoric fluid, highly saline fluid, geothermal fluid, and local seawater. Mixing with seawater occurs prior to fluid discharge on the seafloor. Hydrothermal deposits include veins, breccias, stockworks, crust and stromatolites rich in Mn oxide and silica with Ag minerals

(Morrison et al. 1991). The abundance of chlorine in the studied environment is suggested by the abundance of NaCl in fluid inclusions in the Mapachitos coastal hot springs (Villanueva-Estrada et al. 2012) and Guadalupe prospect (Rodríguez-Díaz et al. 2008). Mn and Ag are transported primarily as uncomplexed ion and chloride complexes, respectively, in acid hydrothermal fluids (200 °C) as the chemical conditions favor high equilibrium constant values; e.g., Mn^{+2} (Gammons and Seward 1996) and $AgCl_4^{-3}$, $AgCl_3^{-2}$, and $AgCl_2^{-}$ (Scaini et al. 1995). In the geochemical modeling conducted by Villanueva-Estrada et al. (2012) the pH is not estimated at depth, but it is assumed that the hydrothermal fluids are characterized by an acidic pH. The chloride complexation occurs under low to moderate acidity, low concentrations of sulfide hydrogen, low H_2S/SO_4 ratios, and < 250 °C temperature (Clark and Williams-Jones 1990).

In a mixture of thermal and saline fluids, the amount of Ag in solution increases with the increase of chloride concentration and variation in the pH. Gammons and Seward (1996) reports that the solubility of the Ag chloro-complexes increases to a pH of 3 and it is reduced to high pH (5) favoring the deposition of Ag in mineral species. This process is suggested for the Guadalupe deposit with Ag concentrations of 64 g/kg at ~ 200 m of depth (Terán-Ortega et al. 1993).

The acid mineralizing solution ascended through the faults causing the argillic alteration of the host rocks and ultimately vent on surface. In the near surface environment, the mineralizing solutions are thought to mix with seawater, as suggested by the relationship between Mg and Na in the hot springs (Fig. 8c) and the geochemical modeling proposed by Villanueva-Estrada et al. (2012). Eventually, the mineralizing solution reaches the surface along the intertidal zone where it is strongly influenced by redox processes and precipitates Mn oxides and Ag minerals (Figs. 9 and 10).

The Mn^{2+} ion in the mineralizing solution can be transported for a considerable distance until the fluids reach the surface, where it precipitates as Mn oxides under oxidizing conditions and near to neutral to alkaline pH (Fig. 10a). Based on Eh-pH diagram, Ag_2S and silver chloro-complexes (AgCl(aq), $AgCl_2^{-}$, $AgCl_3^{-2}$, and $AgCl_4^{-3}$) seem to be the more relevant inorganic species in the system, which is typical of seawater (Barriada et al. 2007). We can observe from the thermodynamic modeling that Ag speciation in seawater will depend more on redox conditions than pH. In the subsurface environment, where the seawater interacts with the rising thermal fluids, the Ag in oxidizing hydrothermal fluids can be transported to the surface in the form of chloro-complexes until it is precipitated by a change to reduced conditions as native silver or acanthite. Under oxidizing conditions, silver is present in solution in the form of the $AgCl_4^{-3}$ ion (Fig. 10b). In this scenario, Ag speciation depends on the Cl/Ag ratio. Under reducing conditions and pH close to neutral, precipitation of Ag_2S and native Ag would be expected (Fig. 10b). Pourbaix diagrams indicate that Mn oxides and Ag minerals can precipitate from the hydrothermal fluid at 65 °C and near-neutral pH under slightly oxidizing to reducing conditions (Fig. 10). This finding further demonstrates the consistency of Mn oxides, acanthite, and native silver mineral assemblage.

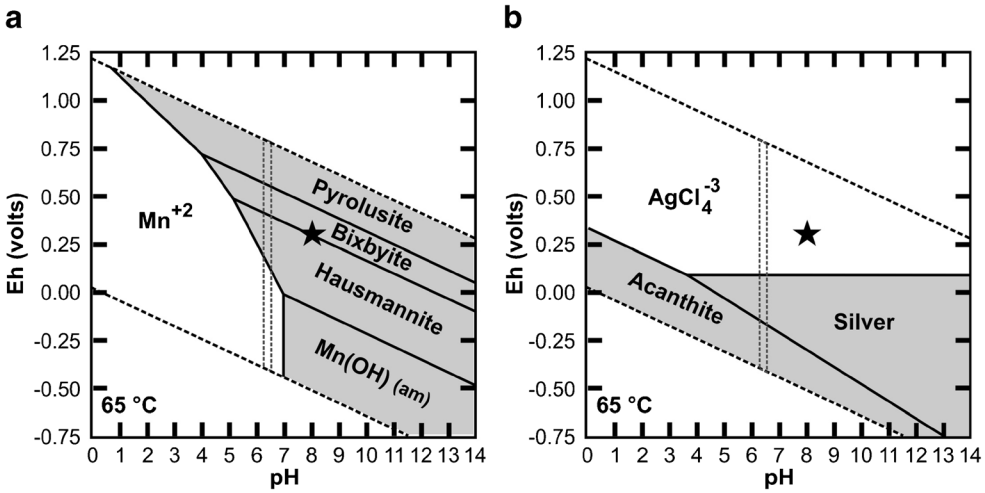

Fig. 10 Pourbaix diagrams showing the speciation of silver and manganese at the discharge temperature for the hot springs. **a** Mn-H_2O system. **b** Ag-H_2O-Cl-SO_4 system. The diagram was constructed using the average discharge temperature (65 °C), the concentration of silver, sulfate, manganese, barium, chloride, and bicarbonate taken from work of Villanueva-Estrada et al. (2012). The activities calculated for these species were $10^{-4.67}$, $10^{-2.27}$, $10^{-0.67}$, $10^{-5.60}$, $10^{-0.07}$, and $10^{-2.61}$, respectively. Fields in gray indicate mineral phases and white fields indicate chemical species in solution. The star indicates the pH and redox potential values of the local seawater (pH = 8, Eh = + 0.3 V). Dotted lines indicate the measured pH interval (6.2–6.5) along the coastal hot springs and the precipitation region of Mn oxides and Ag minerals

Redox and pH conditions for the occurrence of Mn oxides and silver minerals are explained by tidal effects of coastal hot springs. The hydrothermal discharge at low tide and oxidizing conditions causes the deposition of the Mn mineral phases. In fact, Mn deposition is favored by subsurface mixing processes with seawater accompanied by slightly increased pH (Conly et al. 2011). Moreover, organisms can mediate these redox and deposition processes as shown by the presence of Mn stromatolites and well-known documented cases of Mn-biomineralization in hot springs (Mita and Miura 2003; Tebo et al. 2004). In addition, the precipitation of Ag within organic-rich sediments can be favored by the dilution of hydrothermal fluid by seawater (e.g. submarine hot springs of southern California continental borderland, Hein et al. 2005).

Conclusions

- The BC coast has hot springs with discharge temperature of 72 °C and pH ranging from 6.2 to 6.5. Thermal activity is due to a convection-dominated hydrothermal system in an extensional setting controlled by NW-SE faults related to the rifting of the Gulf of California.
- The hot spring deposits contain acanthite and native silver. These occur in a mineral assemblage with opal, todorokite, romanechite, aragonite, Mg-calcite, barite, and pyrite.
- The Mn-Ag hydrothermal deposits are characterized by a Fe and Mn fractionation and are enriched in Si, Ba, Mg, Tl, Sr, Cu, Pb, Sb, As, Zn, Ag, and V.
- Mn-Ag mineralization occurs as a result of subaerial and shallow hydrothermal activity, changes in oxidizing conditions, pH variation, and microbial activity. In these conditions, Mn oxides, acanthite, and native silver can precipitate at near-neutral pH in slightly oxidizing to slightly reducing conditions.
- The active mineralization process of coastal hot springs can be considered as an analogue for Ag-Mn ore deposits of hydrothermal epigenetic origin (e.g., subaerial and shallow submarine hot spring deposits).

Acknowledgments Abigail López, Antoni Camprubí, Cristina Bàncora, and Irvin González Romo are thanked for their assistance and comments during fieldwork. We are grateful to Rosa María Prol-Ledesma providing assistance and advice throughout the project. The authors thank David Blanco Florido and Teresa Pi Puig for conducting the XRD experiments. Juan Tomás Vázquez Ramírez prepared the thin sections. This study forms of A.A.R.D.´s PhD. dissertation. We wish to thank our colleague Juan Luis Carrillo for helpful comments on an earlier version of the manuscript. The paper has benefited from valuable comments and constructive criticism by Thomas Monecke, Christos Kanellopoulos, and Stefanie Brueckner. We also thank Johnson Steven and Estefanny Davalos-Elizondo for their help in reviewing of this article. The research was supported by the Student Mobility Program of UNAM-UGR.

Funding information Funding was provided by the projects CONACyT J-51127-I "Sistemas hidrotermales costeros actuales y fósiles en Baja California: mineralogía, geoquímica, biogeoquímica y sistemática isotópica", SENER-CONACYT CeMie Geo P01, and PAPIIT IG100116.

References

Alfieris D, Voudouris P, Spry PG (2013) Shallow submarine epithermal Pb–Zn–Cu–Au–Ag–Te mineralization on western Milos Island, Aegean Volcanic Arc, Greece: mineralogical, geological and geochemical constraints. Ore Geol Rev 53:159–180

Alldrick DJ (1995) Subaqueous hot spring Au-Ag (G07). In: Lefebure DV, Ray GE (eds) Selected British Columbia Mineral Deposit Profiles, Metallics and Coal. British Columbia Ministry of Employment and Investment, BC Geol Sur, British Columbia, pp 55–58

Arango-Galván C, Prol-Ledesma RM, Torres-Vera MA (2015) Geothermal prospects in the Baja California Peninsula. Geothermics 55:39–57

Barriada JL, Tappin AD, Evans EH, Achterberg EP (2007) Dissolved silver measurements in seawater. Trends Anal Chem 26:809–817

Bartley JK, Knoll AH, Grotzinger JP, Sergeev VN (2000) Lithification and fabric genesis in precipitated stromatolites and associated peritidal carbonates, Mesoproterozoic Billyakh Group, Siberia. In: Grotzinger JP, James NP (eds) Carbonate sedimentation and diagenesis in the evolving Precambrian world. Society for Sedimentary Geology Special Publication 67, pp 59–73

Bastin ES (1948) Mineral relationships in the ores of Pachuca and Real del Monte, Hidalgo, Mexico. Econ Geol 43:53–65

Berger BR, Eimon PL (1983) Conceptual models of epithermal precious metal deposits. In: Shanks WC (ed) Cameron volume on unconventional mineral deposits. Society of Mining Engineers, New York, pp 191–205

Binns RA, Parr JM, Gemmell JB, Whitford DJ, Dean JA (1997) Precious metals in barite-silica chimneys from Franklin seamount, Woodlark basin, Papua New Guinea. Mar Geol 142:119–141

Bishop JL, Madejová J, Komadel P, Fröschl H (2002) The influence of structural Fe, Al and Mg on the infrared OH bands in spectra of dioctahedral smectites. Clay Miner 37:607–616

Blanco-Florido D (2010) Caracterización y diagénesis de las fases silícicas en el sistema hidrotermal de Bahía Concepción, Baja California Sur, México. Dissertation, Instituto de Geofísica, UNAM, 125p

Camprubí A, Canet C, Rodríguez-Díaz AA, Prol-Ledesma RM, Blanco-Florido D, Villanueva RE, López-Sánchez A (2008) Geology, ore deposits and hydrothermal venting in Bahía Concepción, Baja California Sur, Mexico. Island Arc 17:6–25

Canet C, Prol-Ledesma RM, Proenza JA, Rubio-Ramos MA, Forrest MJ, Torres-Vera MA, Rodríguez-Díaz AA (2005) Mn–Ba–Hg mineralization at shallow submarine hydrothermal vents in Bahía Concepción, Baja California Sur, México. Chem Geol 224:96–112

Casarrubias-Unzueta Z, Gómez-López G (1994) Geología y evaluación geotérmica de la zona de Bahía Concepción, Baja California Sur, México. Geotermia, Rev Mex de Geoenergía 10:75–88

Choi JH, Hariya Y (1992) Geochemistry and depositional environment of Mn oxide deposits in the Tokoro Belt, northeastern Hokkaido, Japan. Econ Geol 87:1265–1274

Clark JR, Williams-Jones AE (1990) Analogues of epithermal gold–silver deposition in geothermal well scales. Nature 346:644–645

Clark RN, Swayze GA, Wise RA, Livo KE, Hoefen TM, Kokaly RF, Sutley SJ (2007) USGS digital spectral library splib06a. USGS

Digital Data Series: 231. http://speclab.cr.usgs.gov. Accessed 02 December 2017

Conly AG, Scott SD, Bellon H (2011) Metalliferous manganese oxide mineralization associated with the Boleo Cu-Co-Zn district, Mexico. Econ Geol 106:1173–1196

Crespo A, Lunar R (1997) Terrestrial hot-spring Co-rich Mn mineralization in the Pliocene–Quaternary Calatrava region (central Spain). In Nicholson K, Hein JR, Bühn B, Dasgupta S (eds) Manganese mineralization, geochemistry and mineralogy of terrestrial and marine deposits. Geological Society Special Publication 119, London, pp 253–264

del Rio-Salas R, Ruiz J, Ochoa-Landín L, Noriega O, Barra F, Meza-Figueroa D, Paz-Moreno F (2008) Geology, Geochemistry and Re–Os systematics of manganese deposits from the Santa Rosalía Basin and adjacent areas in Baja California Sur, México. Mineral Deposita 43:467–482

Dolenec T (2003) Todorokite –a 10Å manganate from the Jabuka Pit (Central Adriatic). Mater Geoenviron 50:453–466

Gammons CH, Seward TM (1996) Stability of manganese (II) chloride complexes from 25 to 300°C. Geochim Cosmochim Acta 60:4295–4311

Gómez-Caballero JA, Villaseñor-Cabral MG, Santiago-Jacinto P, Ponce-Abad F (2010) Hypogene Ba-rich todorokite and associated nanometric native silver in the San Miguel Tenango Zacatlán, Puebla, Mexico. Can Mineral 48:1237–1253

Granina L, Klerkx J, Callender E, Leermakers M, Golobokova LP (2007) Peculiarities of the bottom sediments and porewaters in the area of hydrothermal venting in Lake Baikal (Frolikha Bay). Russ Geol Geophys 3:305–316

Hein JR, Stamatakis MG, Dowling JS (2000) Trace metal-rich Quaternary hydrothermal manganese oxide and barite deposit, Milos Island, Greece. Appl Earth Sci 109:67–76

Hein JR, Koschinsky A, McIntyre BR (2005) Mercury-and silver-rich ferromanganese oxides, southern California borderland: deposit model and environmental implications. Econ Geol 100:1151–1168

Herdianita NR, Rogers KA, Browne PRL (2000) Routine instrumental procedures to characterize the mineralogy of modern and ancient silica sinters. Geothermics 29:65–81

Hewett DF (1968) Silver in veins of hypogene manganese oxides, U.S. Department of the Interior. Geol Surv Circular 553:1–9

Jones B, Renaut RW, Rosen MR (2001) Biogenicity of gold-and silver-bearing siliceous sinters forming in hot (75 °C) anaerobic spring-waters of Champagne Pool, Waiotapu, North Island, New Zealand. J Geol Soc Lond 158:895–911

Kanellopoulos C, Mitropoulos P, Valsami-Jones E, Voudouris P (2017) A new terrestrial active mineralizing hydrothermal system associated with ore-bearing travertines in Greece (northern Euboea Island and Sperchios area). J Geochem Explor 179:9–24

Kilias SP, Naden J, Cheliotis I, Shepherd TJ, Constandinidou H, Crossing J, Simos I (2001) Epithermal gold mineralisation in the active Aegean volcanic arc: the Profitis Ilias deposit, Milos Island, Greece. Mineral Deposita 36:32–44

Lachenbruch AH, Sass JH, Galanis SP (1985) Heat flow in southernmost California and the origin of the Salton trough. J Geophys Res Solid Earth 90:6709–6736

Leal PR, Correa MJ, Ametrano SJ, Etcheverry RO, de Brodtkorb MK (2008) The manganese deposit of the Pampean Ranges, Argentina. Can Mineral 46:1215–1233

Levard C, Hotze EM, Lowry GV, Brown GE (2012) Environmental transformations of silver nanoparticles: impact on stability and toxicity. Environ Sci Technol 46:6900–6914

Liakopoulos A, Glasby GP, Papavassiliou CT, Boulegue J (2001) Nature and origin of the Vani manganese deposit, Milos, Greece: an overview. Ore Geol Rev 18:181–209

Lozano R, Bernal JP (2005) Assessment of a new set of geochemical reference materials for XRF major and trace element analysis. Rev Mex Cienc Geol 22:329–344

Lugović B, Šegvić B, Šegvić T (2008) Mn-crust todorokite mineralization on SW backshore Cretaceous limestones from the island of Dugi Otok (Central Adriatic, Croatia). Acta Adriat 49:53–63

Lynne BY, Campbell KA, Moore J, Browne PRL (2005) Diagenesis of 1900-year-old siliceous sinter (opal-A to quartz) at Opal Mound, Roosevelt Hot Springs, Utah, U.S.A. Sediment Geol 119:249–278

Mandernack KW, Fogel ML, Tebo BM, Usui A (1995) Oxygen isotope analyses of chemically and microbially produced manganese oxides and manganates. Geochim Cosmochim Acta 59:4409–4425

McKeown N, Bishop JL, Cuadros J, Hillier S, Amador E, Makarewicz HD, Silver EA (2011) Interpretation of reflectance spectra of clay mineral-silica mixtures: implications for Martian clay mineralogy at Mawrth Vallis. Clay Clay Miner 59:400–415

Mita N, Miura H (2003) Evidence of microbial formation of manganese wads at the Asahidake hot spring in Hokkaido, Japan. Resour Geol 53:233–238

Miura H, Hariya Y (1997) Recent manganese oxide deposits in Hokkaido, Japan. In Nicholson K, Hein JR, Bühn B, Dasgupta S (eds) Manganese mineralization: geochemistry and mineralogy of terrestrial and marine deposits. Geological Society Special Publication 119, London, pp 281–299

Montes-Hernandez G, Findling N, Renard F (2016) Dissolution-precipitation reactions controlling fast formation of dolomite under hydrothermal conditions. Appl Geochem 73:169–177

Morrison GW, Rose WJ, Jaireth S (1991) Geological and geochemical controls on the silver (fineness) of gold in gold-silver deposits. Ore Geol Rev 6:313–364

Nicholson K (1992) Contrasting mineralogical—geochemical signatures of manganese oxides: genesis to metallogenesis. Econ Geol 87: 1253–1264

Ostwald J (1982) Some observations on todorokites from marine and terrestrial environments. Mineral Mag 46:253–256

Papavassiliou K, Voudouris P, Kanellopoulos C, Glasby G, Alfieris D, Mitsis I (2017) New geochemical and mineralogical constraints on the genesis of the Vani hydrothermal manganese deposit at NW Milos island, Greece: comparison with the Aspro Gialoudi deposit and implications for the formation of the Milos manganese mineralization. Ore Geol Rev 80:594–611

Post JE (1999) Manganese oxide minerals: crystal structures and economic and environmental significance. Proc Natl Acad Sci 96:3447–3454

Prol-Ledesma RM, Canet C, Torres-Vera MA, Forrest MJ, Armienta MA (2004) Vent fluid chemistry in Bahía Concepción coastal submarine hydrothermal system, Baja California Sur, Mexico. J Volcanol Geotherm Res 137:311–328

Riding R (2011) Microbialites, stromatolites, and thrombolites. In: Reitner J, Thiel V (eds) Encyclopedia of Geobiology. Springer, Netherlands, pp 635–654

Rodríguez-Díaz AA, Canet C, Gervilla F, González-Partida E, Blanco-Florido D, Villanueva-Estrada RE, Morales-Ruano S, Prol-Ledesma RM, Camprubí A (2008) Metalogenia del área mineralizada en manganeso de Bahía Concepción, Baja California Sur, México. Unión Geof Mex Anual Meet Abstr Geos 28:169–170

Rodríguez-Díaz AA, Blanco-Florido D, Canet C, Gervilla-Linares F, González-Partida E, Prol-Ledesma RM, Morales-Ruano S, García-Vallès M (2010) Metalogenia del depósito de manganeso Santa Rosa, Baja California Sur, México. Bol Soc Geol Mex 62:141–159

Rodríguez-Martínez M, Heim C, Quéric NV, Reitner J (2011) Frutexites. In: Reitner J, Thiel V (eds) Encyclopedia of Geobiology. Springer, Netherlands, pp 396–401

Scaini MJ, Bancroft GM, Lorimer JW, Madox LM (1995) The interaction of aqueous silver species with sulphur-containing minerals as

studied by XPS, AES, SEM, and electrochemistry. Geochim Cosmochim Acta 59:2733–2747

Sillitoe RH (1975) Lead-silver, manganese, and native sulfur mineralization within a stratovolcano, El Queva, Northwest Argentina. Econ Geol 70:1190–1201

Sinisi R, Mameli P, Mongelli G, Oggiano G (2012) Different Mn-ores in a continental arc setting: geochemical and mineralogical evidences from tertiary deposits of Sardinia (Italy). Ore Geol Rev 47:110–125

Tebo BM, Bargar JR, Clement BG, Dick GJ, Murray KJ, Parker D, Verity R, Webb SM (2004) Biogenic manganese oxides: properties and mechanisms of formation. Annu Rev Earth Planet Sci 32:287–328

Terán-Ortega LA, Ávalos-Zermeño A, Sánchez-Alvarado P (1993) Informe de definición del Prospecto Las Mantitas, Anomalía Pilares, Área Bahía Concepción, Zona el Azufre, Municipio de Mulegé, Estado de Baja California Sur, Cuarta etapa. Consejo de Recursos Minerales, Reporte Técnico, Mexico

Toth JR (1980) Deposition of submarine crusts rich in manganese and iron. Geol Soc Am Bull 91:44–54

Usui A, Mita N (1995) Geochemistry and mineralogy of a modern buserite deposit from a hot spring in Hokkaido, Japan. Clay Clay Miner 43:116–127

Villanueva-Estrada RE, Prol-Ledesma RM, Rodríguez-Díaz AA, Canet C, Torres-Alvarado IS, González-Partida E (2012) Geochemical processes in an active shallow submarine hydrothermal system, Bahía Concepción, México: mixing or boiling? Int Geol Rev 52: 907–919

Villanueva-Estrada RE, Prol-Ledesma RM, Rodríguez-Díaz AA, Canet C, Armienta MA (2013) Arsenic in hot springs of Bahía Concepción, Baja California Peninsula, México. Chem Geol 348: 27–36